Preprints (www.preprints.org) | NOT PEER-REVIEWED | Posted: 9 October 2020 doi:10.20944/preprints202010.0200.v1

A four-dimensional computational model of dynamic contrast-enhanced magnetic resonance imaging measurement of subtle blood-brain barrier leakage

Jose Bernal[1], Maria d. C. Valdés-Hernández[1], Javier Escudero[2], Anna K. Heye[1], Eleni Sakka[1], Paul A. Armitage[3], Stephen Makin[4], Rhian M. Touyz[5], Joanna M. Wardlaw[1], Michael J. Thrippleton[1]

[1]Centre for Clinical Brain Sciences, Dementia Research Institute at the University of Edinburgh, Edinburgh EH16 4SB, UK

[2]School of Engineering, University of Edinburgh, Edinburgh EH9 3FB, UK

[3]Academic Unit of Radiology, University of Sheffield, Sheffield S10 2RX, UK

[4]University of Aberdeen, Centre for Rural Health, Inverness, UK

[5]Institute of Cardiovascular and Medical Sciences, University of Glasgow, Glasgow G12 8TA, UK

Abstract

Dynamic contrast-enhanced MRI (DCE-MRI) is increasingly used to quantify and map the spatial distribution of blood-brain barrier (BBB) leakage in neurodegenerative disease, including cerebral small vessel disease and dementia. However, the subtle nature of leakage and resulting small signal changes make quantification challenging. While simplified one-dimensional simulations have probed the impact of noise, scanner drift, and model assumptions, the impact of spatio-temporal effects such as gross motion, *k*-space sampling and motion artefacts on parametric leakage maps has been overlooked. Moreover, evidence on which to base the design of imaging protocols is lacking due to practical difficulties and the lack of a reference method. To address these problems, we present an open-source computational model of the DCE-MRI acquisition process for generating four dimensional Digital Reference Objects (DROs), using a high-resolution brain atlas and incorporating realistic patient motion, extra-cerebral signals, noise and *k*-space sampling. Simulations using the DROs demonstrated a dominant influence of spatio-temporal effects on both the visual appearance of parameter maps and on measured tissue leakage rates. The computational model permits greater understanding of the sensitivity and limitations of subtle BBB leakage measurement and provides a non-invasive means of testing and optimising imaging protocols for future studies.

Keywords

Digital reference object; Blood-brain barrier permeability; DCE-MRI; Spatio-temporal imaging artefacts; Endothelial dysfunction; Cerebral small vessel disease

 doi:10.20944/preprints202010.0200.v1

1 Introduction

DCE-MRI is the most commonly used technique for assessing breakdown of the blood-brain barrier (BBB) in neurological diseases, such as multiple sclerosis, brain tumours, stroke and small vessel diseases. By detecting the signal changes following intravenous injection of a gadolinium-based contrast agent (GBCA), quantitative estimates (K^{Trans} or PS) of its leakage across the BBB are obtained. While DCE-MRI is long-established in the context of high permeability, application of the technique is now rapidly growing in diseases such as cerebral small vessel diseases (SVD) and dementia, where BBB breakdown is typically very subtle. For example, recent studies have shown elevated BBB leakage in the normal-appearing white matter (NAWM) of patients with greater SVD burden, suggesting a possible role for BBB breakdown in the development of radiological signs and eventual clinical symptoms of the disease [1]. In the field of Alzheimer's disease, another recent study reported increased BBB leakage among APOE4 gene carriers, including those without cognitive impairment [2].

Such advanced neuroimaging studies are highly valuable for understanding these diseases, whose pathophysiology is poorly understood [3] and which have a major clinical and societal impact. However, while DCE-MRI is currently the standard imaging approach to investigating BBB dysfunction, the extremely low level of leakage and consequent small signal changes (typically a few percent) limit its accuracy and precision. Furthermore, the lack of a convenient reference method, and ethical and safety considerations around GBCA administration, make it difficult to assess measurement reliability and impede protocol optimisation, as summarised in two recent review and recommendation papers [4], [5]. Previous computational studies have attempted to address this problem by applying a Monte-Carlo simulation approach to generate synthetic one-dimensional time-signal data for tissues with pre-specified leakage values, yielding important insights into the effects of pharmacokinetic model selection, signal stability and noise on the accuracy and precision of "permeability" mapping [6]–[9]. However, this approach overlooks spatio-temporal effects, such as patient motion, partial volume effect and ringing artefacts, which may have a significant impact on the appearance of parameter maps [6] and, potentially, on reported leakage rates. The assessment of these spatio-temporal considerations is more conceptually and computationally demanding since both the measurement process and the participant must be simulated in the three spatial dimensions and time.

In this work, we propose an open-source computational model that uses *in-vivo* volunteer and patient data for mimicking the four-dimensional DCE-MRI acquisition process to evaluate the aforementioned confounds and enable better protocol optimisation in the future. We used a publically available high-resolution atlas to generate realistic head and neck anatomy [10] and combined it with motion parameters and signal enhancement properties obtained from a large cohort of SVD patients [1]. We

Preprints (www.preprints.org) | NOT PEER-REVIEWED | Posted: 9 October 2020 doi:10.20944/preprints202010.0200.v1

used the resulting digital reference objects (DROs) to simulate the appearance of leakage maps and measured leakage values in healthy and diseased brain tissue under realistic experimental conditions, including *k*-space sampling, noise, gross motion and motion artefacts. Finally, we explored the potential of image processing methods to enhance the accuracy of BBB leakage measurements.

2 Materials and methods

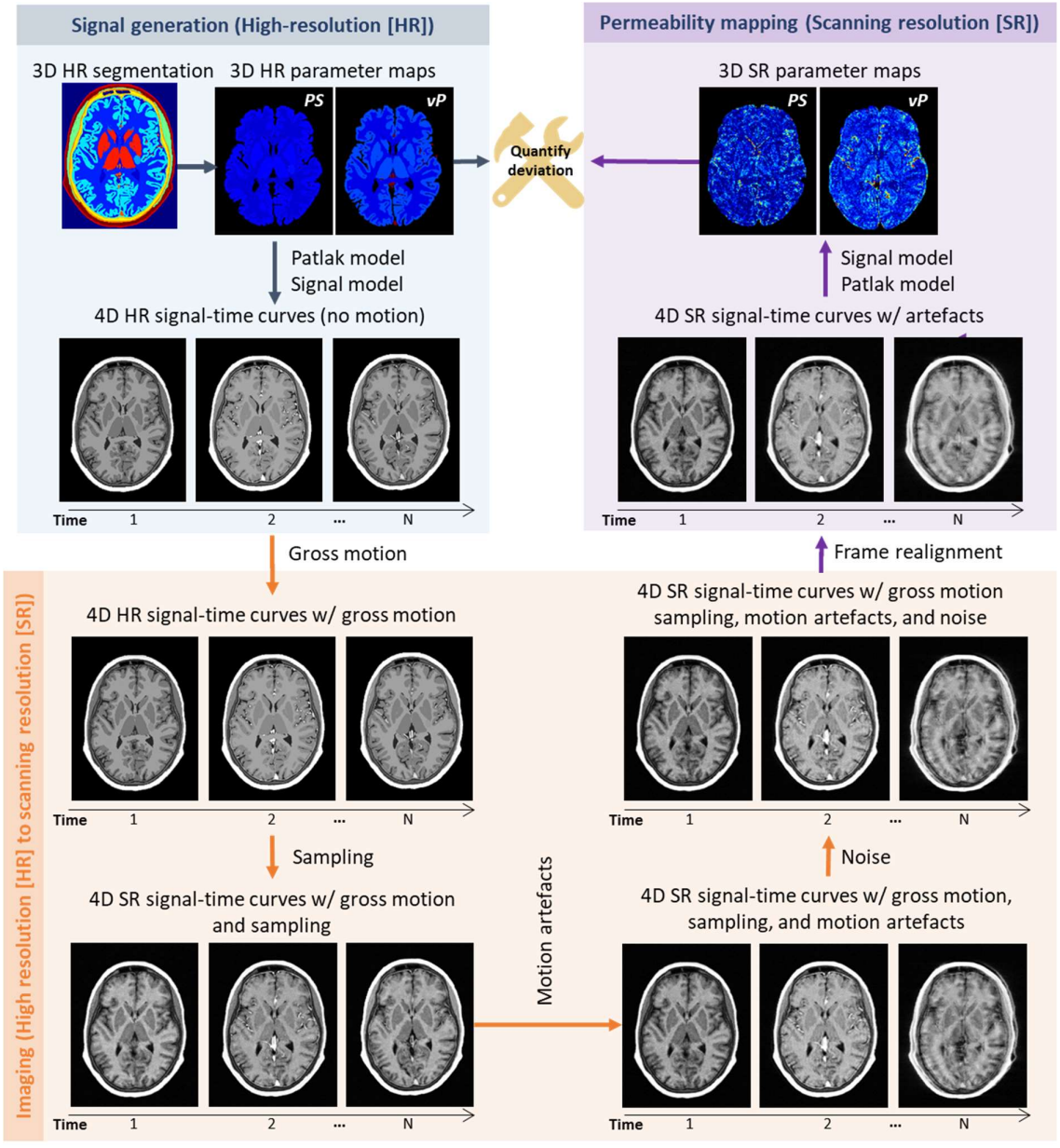

Figure 1. Proposed computational framework for generating 4D dynamic contrast-enhanced magnetic resonance images and simulating PS mapping under realistic conditions. PS: permeability-surface area product. v_P: fractional blood plasma volume.

Preprints (www.preprints.org) | NOT PEER-REVIEWED | Posted: 9 October 2020 doi:10.20944/preprints202010.0200.v1

2.1 Digital reference object

We identified two main requirements for devising a realistic computation model for evaluating subtle BBB leakage measurement. First, it should contain both healthy and pathological brain tissues as well as non-brain tissues that are commonly excluded in simulations. Second, it should simulate aspects of the acquisition process that are known or expected to affect the appearance of DCE-MRI parameter maps, such as motion and truncation artefacts.

We simulated the DCE-MRI signal generation, measurement and analysis processes via the steps illustrated in Figure 1 and described in detail below. Briefly, we used a high-resolution head model with pre-specified MR and ground-truth pharmacokinetic properties to generate four-dimensional time-signal data. We applied spatial transformations derived from *in-vivo* scan data to simulate gross motion and motion artefacts, resampled the resulting data in *k*-space to yield "acquired" images at lower resolution and added random noise. We post-processed and analysed these scans to obtain simulated pharmacokinetic parameter maps. Code for generating the DROs is freely available at https://github.com/joseabernal/BrainDCEDRO.

2.1.1 Ground truth

We developed the signal model based on a three-dimensional high-resolution (0.5-mm isotropic), comprehensively-labelled and publicly-available human head and neck atlas [10][1]. The atlas is particularly suitable for application to DCE-MRI because a wide range of segmented tissues including both brain tissues and nearby GBCA-enhancing structures, such as vessels and muscle, are labelled (Figure 2). We combined some of the tissue classes to reduce complexity and because the enhancement properties of each are not well known. To better represent the ageing brain, we added two regions of neuropathology associated with elevated permeability, specifically white matter hyperintensities and lacunar stroke lesions, using spatial occurrence templates extracted from patient data (https://doi.org/10.7488/ds/2716). In total, our computational model comprised 16 regions of interest. We assigned values for the equilibrium signal intensity S_0, pre-contrast longitudinal relaxation time T_{10}, blood plasma volume fraction v_P and permeability surface area product PS to each tissue class.

[1] The MIDA human head model can be downloaded from *www.itis.ethz.ch/MIDA/*

Preprints (www.preprints.org) | NOT PEER-REVIEWED | Posted: 9 October 2020 doi:10.20944/preprints202010.0200.v1

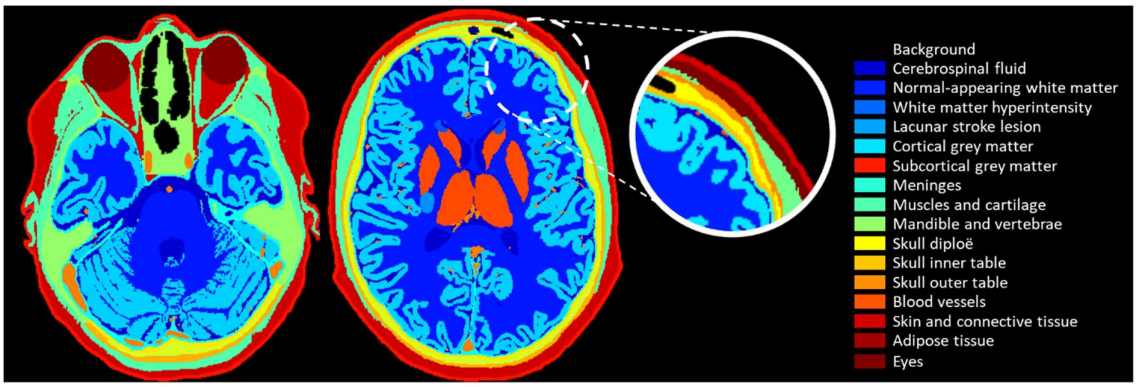

Figure 2. Tissue classes included in our computational model and used to generate 4D high-resolution digital reference objects. We considered 16 tissues, comprising cerebrospinal fluid; normal-appearing white matter; white matter hyperintensities; stroke lesion; cortical grey matter; subcortical grey matter; meninges; muscle and cartilage; mandible and vertebrae; skull diploe; skull inner table; skull outer table; blood vessels; skin and connective tissue; adipose tissue; and eyes.

2.1.2 Generation of high-resolution 4D signal

We simulated the GBCA concentration over time for each location within the high-resolution reference object using the Patlak model [11], which has previously been shown to closely describe tracer kinetic behaviour in the slow leakage regime at low temporal resolution [6], [12]:

$$C_t[t] = v_p c_p[t] + PS \int_0^t c_p[t'] \, \mathrm{d}t',$$

where $c_p[t]$ represents the specified GBCA time-concentration function in blood plasma or arterial input function (AIF) and $C_t[t]$ is the total tissue GBCA concentration. Although it would be possible to use a more complex pharmacokinetic model to simulate ground-truth concentration, by using the Patlak model we ensured that any errors in the fitted parameters are caused by the measurement process, which is the focus of this work. To simulate signal within tissues that do not have a BBB we used time-signal curves measured directly from in-vivo patient data.

Having computed the concentration-time curves per voxel, we calculated the corresponding signal-time curves using the spoiled gradient echo signal formula:

$$S[t] = S_0 \frac{\left(1 - e^{-TR/T_1[t]}\right) \sin\theta_{FA}}{1 - e^{-TR/T_1[t]} \cos\theta_{FA}} \cdot e^{-TE/T_2^*[t]},$$

where TR and TE represent the repetition and echo times respectively, θ_{FA} is the excitation flip angle and $T_2^*[t]$ is the effective transverse relaxation time at time t. The relaxation rate was assumed to vary linearly with the contrast agent concentration:

$$\frac{1}{T_i[t]} = \frac{1}{T_{i0}} + r_i \cdot c_t[t], i = 1, 2,$$

Preprints (www.preprints.org) | NOT PEER-REVIEWED | Posted: 9 October 2020 doi:10.20944/preprints202010.0200.v1

where r_i is the relaxivity. Time-signal curves were thus generated for each location within the three-dimensional high-resolution model.

2.1.3 Simulation of acquired data and motion effects

We randomised the initial head position by applying a rigid-body spatial transform to the DRO, such that each degree of freedom was randomly distributed with uniform probability over the range ±5° for rotations and ±2.5 mm for translations. We simulated gross patient movement during the subsequent DCE-MRI acquisition by applying a rigid-body transformation to the DRO prior to each time frame.

We then calculated the *k*-space representation of the high-resolution DRO for each time frame as the three-dimensional inverse Fourier transform. We resampled this to obtain *k*-space data with the acquired field of view and spatial resolution. We simulated motion artefacts, which typically manifest as blurring, ringing and/or ghosting, using the approach of [13]. In a nutshell, we generated a composite *k*-space image for each frame in which a random proportion of the *k*-space lines were acquired with the head in its initial position (i.e. that at the end of the previous time frame) and the remaining lines acquired with the head in its subsequent position (i.e. that at the start of the next time frame). We assumed three-dimensional Cartesian *k*-space sampling and suppressed signals from outside the field of view in the frequency- and slice-encoding directions to simulate band filtering and slab-selective excitation, respectively. Finally, we applied a three-dimensional Fourier transform to the *k*-space image and added additive white Gaussian noise (AWGN) to the resulting magnitude image to yield the "acquired" four-dimensional DRO image.

2.1.4 Analysis of simulated DRO images

We processed the simulated DCE-MRI data following the approach described previously in [6]. Briefly, we spatially realigned all frames using MCFLIRT [14], computed enhancement and GBCA concentration profiles for each voxel, and fitted time-concentration curves to the Patlak model using multiple-linear regression to obtain voxelwise maps of estimated v_P and *PS*.

To obtain summary parametric measures for each tissue, we performed the following steps to generate the segmentation map in the acquired image space. First, we registered the high-resolution pre-contrast T1w image to the acquired one. Second, we applied the resulting affine transformation matrix to the binary mask of each tissue class, interpolating with a cubic approximation. Third, for each voxel, we assigned the label corresponding to the tissue class with the maximum probability, resulting in a region of interest (ROI) binary mask for each tissue.

Preprints (www.preprints.org) | NOT PEER-REVIEWED | Posted: 9 October 2020 doi:10.20944/preprints202010.0200.v1

Using the produced segmentation map, we generated a T_{10} map at the acquired resolution using the average region-wise values extracted from our patient cohort. For each tissue we calculated mean and median v_P and *PS* values using two approaches: fitting of the ROI-averaged signal and averaging over the parametric maps.

2.2 In-silico experiments

2.2.1 MR protocol parameters and input data for generating DROs

We explored the qualitative impact of experimental factors on leakage mapping and the quantitative impact on parameter estimates using DCE-MRI data simulated using the framework described above. As a representative MR protocol used for measuring low-level BBB leakage, we simulated the acquisition protocol used in a recent DCE-MRI study of SVD patients [1]. Briefly, 201 patients with lacunar or cortical mild stroke recruited prospectively in the Mild Stroke Study 2 (MSS2) were scanned at 1.5 T using a 3D T1-w spoiled gradient echo sequence (TR/TE = 8.24/3.1 ms, flip angle 12°, 24 x 24cm FoV, 0.9375 x 1.25 x 4 mm acquired resolution, 73 s temporal resolution, intravenous bolus injection of 0.1 mmol/kg gadoterate meglumine) for DCE-MRI, in addition to T_{10} measurement. The patients had a wide range of extents of neuroimaging features of SVD and were carefully phenotyped at presentation, recruitment and at up to 3 years of follow-up. The in-vivo study was conducted following Research Ethics Committee approval (ref. 09/81101/54) and according to the principles expressed in the Declaration of Helsinki; all patients gave written informed consent. Full details of the study protocol, image acquisition and processing, and results are given in [1], [6], [15].

Average T_{10}, v_P and *PS* values for NAWM, GM and WMH obtained from this study were used as ground-truth values for generation of DROs. For vessels, we used a $PS = 0$ and $v_P = 1\text{-Hct}$ (Hct was assumed to be 0.45). For all non-brain regions, an image analyst sampled acquired signal-time curves of these structures manually under the supervision of an experienced neuroradiologist. We extracted the signal intensity profiles of meninges, skin and muscle, mandible and vertebrae, eyes and skull diploe, inner and outer tables from DCE-MRI scans of patients in the study cohort. A population-average vascular input function based the same data was used in simulations.

To generate realistic motion effects in our simulations, including examples of low, moderate and high degrees of motion, we used transformation matrices determined during spatial realignment of the above patient scans. We generated 201 DROs using a different motion trajectory each time, and randomised starting position and spatial noise for each run..

To achieve a realistic spatial noise level, we measured an in-vivo spatial signal-to-noise ratio of 91.5 for NAWM and applied the corresponding noise level (scaled to match the simulated signal) to all voxels in the simulate images.

Preprints (www.preprints.org) | NOT PEER-REVIEWED | Posted: 9 October 2020 doi:10.20944/preprints202010.0200.v1

2.2.2 Experiments and reporting

We generated and analysed synthetic DCE-MRI data for the SVD patient population as described above. We first performed *in-silico* experiments to investigate the impact of *k*-space sampling, gross motion, motion artefacts and AWGN on the appearance of *PS* parametric maps. To further investigate these effects, we performed simulations for different initial head positions and degrees of head motion; to investigate the influence of non-brain GBCA uptake, we run additional experiments with and without enhancement of extra-cerebral tissues. To evaluate the possible impact on study findings, we generated and analysed 201 DROs, determining *PS* values for each DRO and tissue, using various processing approaches (mean signal, median signal, mean parameter, median parameter and erosion of the ROIs). For each approach, we obtained the *PS* distribution across all 201 DROs, reporting the median and interquartile range (IQR) values (RStudio v1.2.5019 with R v3.5.1).

We ran all experiments on a 189GB RAM computer running Scientific Linux 7.3 (Nitrogen). Each simulation took approximately 20 min.

3 Results

3.1 Qualitative appearance of *PS* maps

Figure 3 shows *PS* parametric maps measured from a generated DRO and showing the cumulative effects of sampling (i.e. truncation in *k*-space), gross patient motion, motion artefact and additive white Gaussian noise. The DRO was generated assuming uniform *PS* within each brain tissue class. Data sampling results in ringing artefacts in all three spatial dimensions, particularly in the slice direction where the voxel dimension is highest; nevertheless, differential leakage between tissues is resolved, including elevated *PS* in the WMHs and stroke lesion. However, inclusion of moderate patient motion obscures tissue differences and induces artefactual features close to tissue boundaries and vessels, and additional ringing artefacts. The additional effect of AWGN is small, with motion effects dominating the visual appearance. It is noteworthy that, while the motion effects on *PS* maps are severe, the degree of head motion is moderate and the impact on the underlying T1w images is seen to be small in comparison. To further illustrate the implications of motion, Figure 4 shows simulated *PS* maps in the basal ganglia region, where areas of falsely increased (and decreased) periventricular leakage appear and become more apparent with increasing degree of head movement.

Preprints (www.preprints.org) | NOT PEER-REVIEWED | Posted: 9 October 2020 doi:10.20944/preprints202010.0200.v1

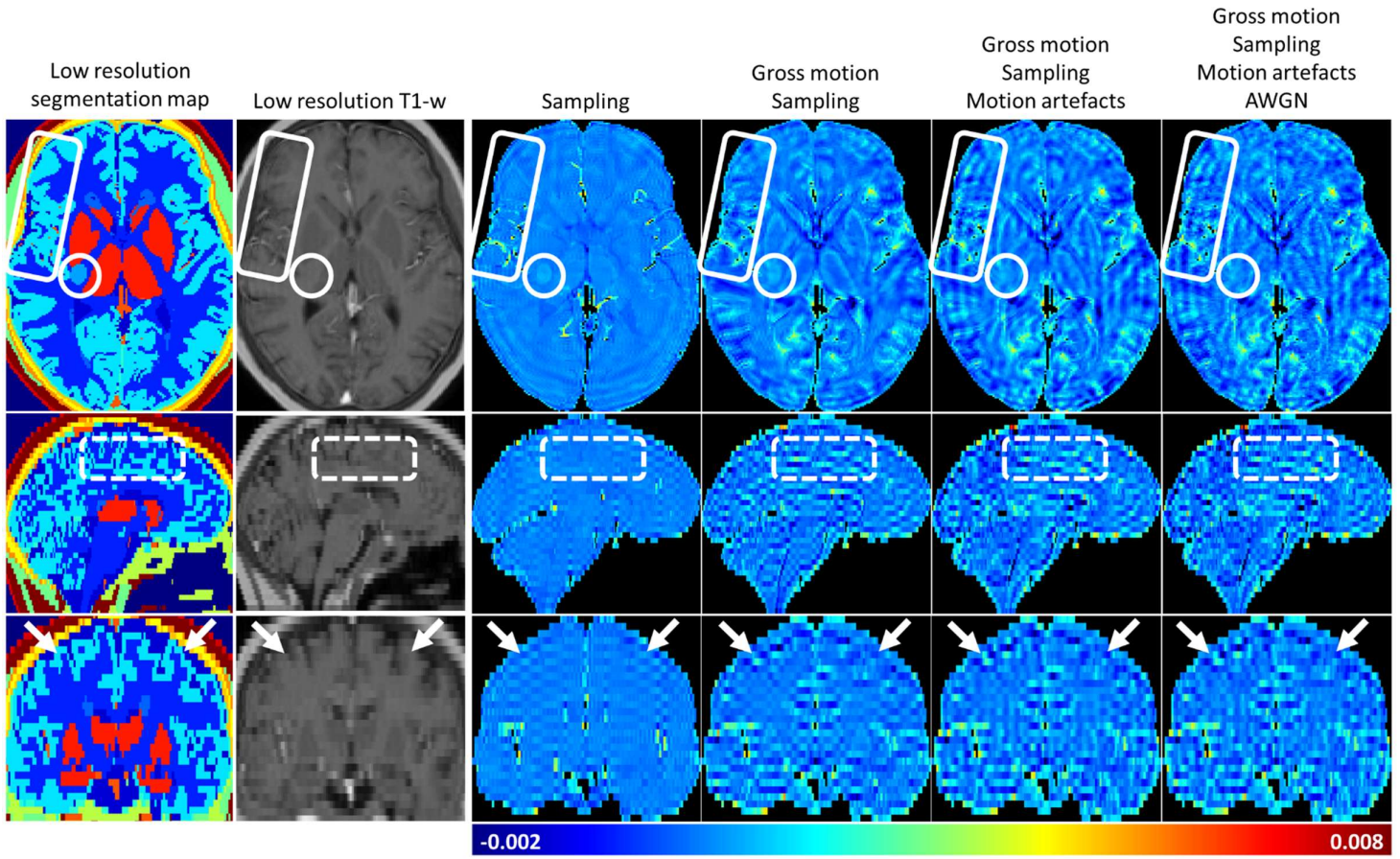

Figure 3. PS maps measured using the DRO when affected by k-space sampling, gross motion, motion artefacts and additive white Gaussian noise (AWGN) progressively. k-space undersampling leads to sinc-like oscillations in the permeability maps (white arrows in coronal view), which are particularly evident in the z-direction (superior to inferior). Gross motion produced noticeable deviations and artefactual features in all brain regions, particularly around tissue interfaces (white dashed rectangle in sagittal view). Motion artefacts produced additional ringing artefacts that propagated from the signal-time data to the PS maps (solid white rectangle in axial view). A stroke lesion with elevated leakage is visible in the absence of motion (solid white circle in axial view) but obscured due to motion effects. Note that the artefacts observed in the PS maps appear at only a low level in the underlying T1w images (second column).

Preprints (www.preprints.org) | NOT PEER-REVIEWED | Posted: 9 October 2020 doi:10.20944/preprints202010.0200.v1

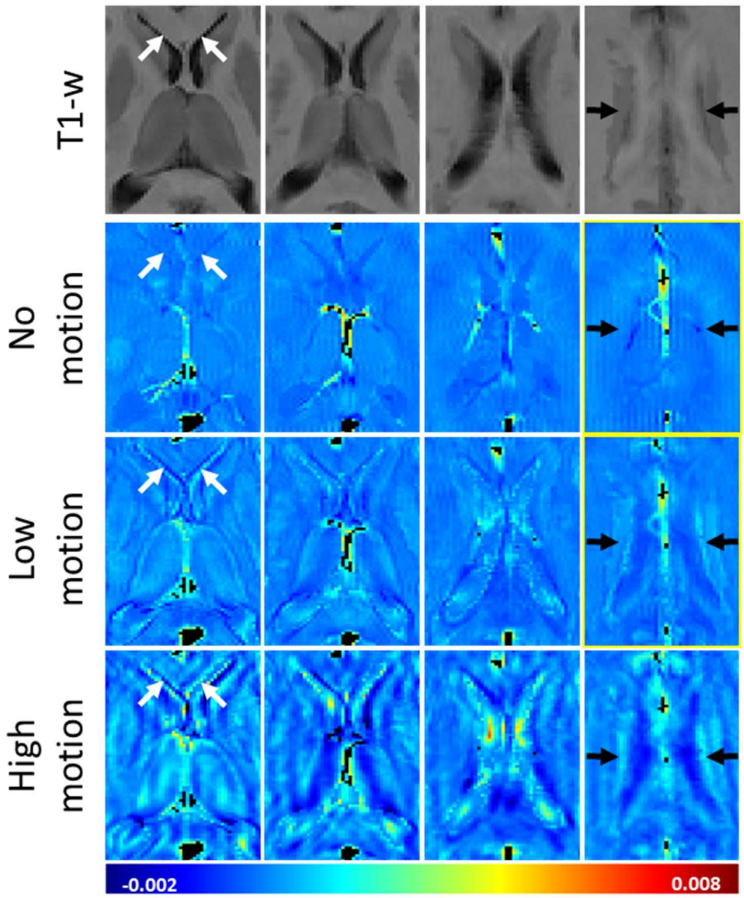

Figure 4. Artefactual periventricular leakage due to sampling and motion effects. From top to bottom, T1-w scan and permeability-surface area product maps generated with no, low, and high levels of patient motion, respectively. The artefactual PS features are evident in the genu of the corpus callosum (white arrows) and in the adjacent supraventricular corona radiata (black arrows), where white matter hyperintensities frequently occur. Such artefacts, caused by sampling and motion effects, might potentially be confused with "periventricular BBB dysfunction" due to subtle pathology.

To quantify these effects, we created histograms to show the distribution of *PS* within each tissue for a single DRO (simulated with low-level patient motion, Figure 5). Although we defined each tissue to have a uniform *PS*, *k*-space sampling generates a broad distribution of values, which becomes broader when we incorporated motion and additive white Gaussian noise in the DRO. In addition to causing a distribution of *PS* values, both sampling and gross motion affect central tendency values (i.e. mean or median), especially for cortical grey matter where the bias was 1.82×10^{-4} min^{-1} (48 %) relative to the ground-truth value. The effects simulated can also result in non-physical negative *PS* values in some voxels.

Preprints (www.preprints.org) | NOT PEER-REVIEWED | Posted: 9 October 2020 doi:10.20944/preprints202010.0200.v1

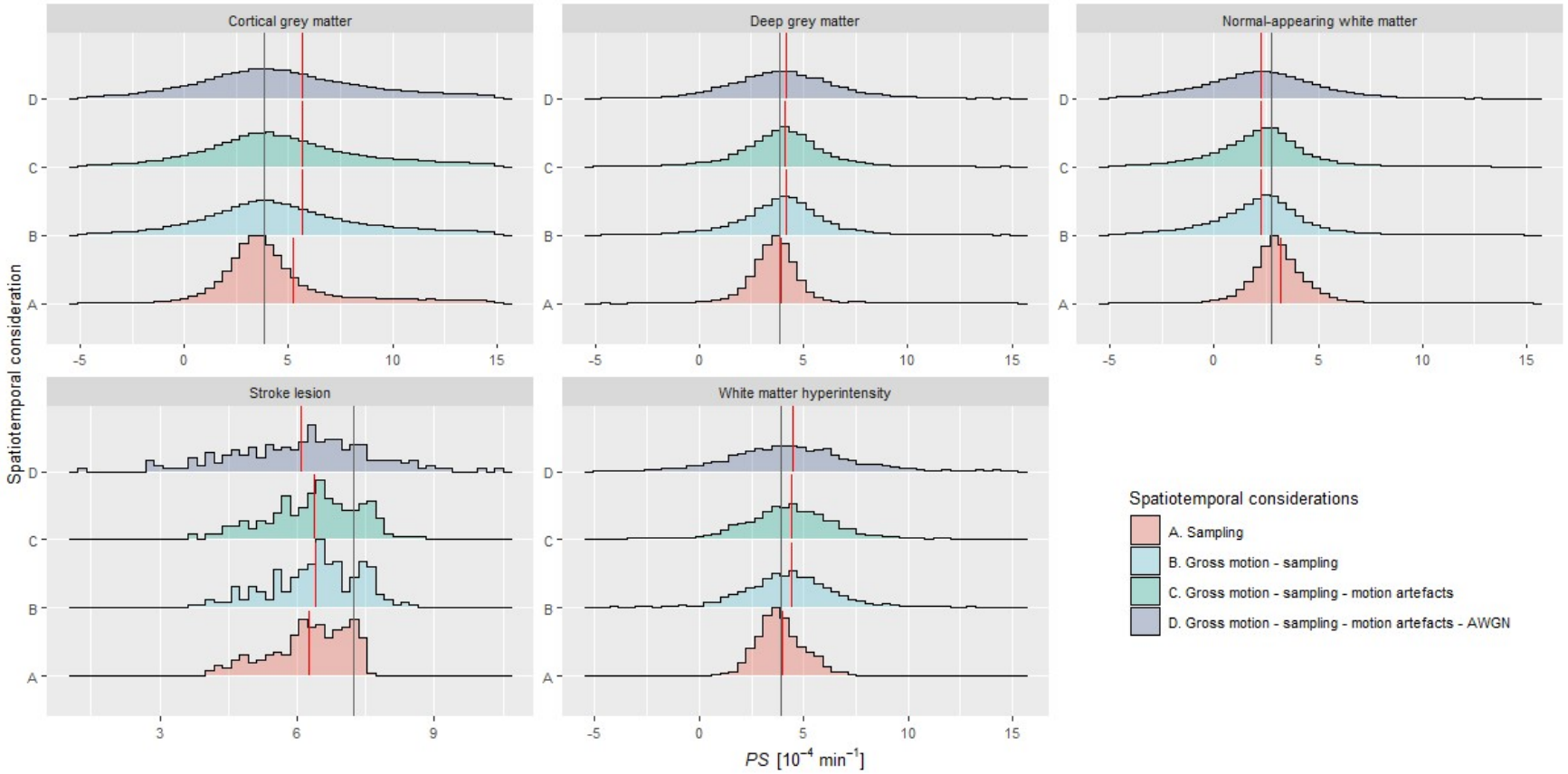

Figure 5. Distribution of measured PS values for each tissue of interest as we induced spatio-temporal effects progressively in a single patient (data correspond to 'Low motion' images shown in Figure 4). The vertical lines depict the ground truth (grey) and mean (red) PS values. AWGN: additive white Gaussian noise.

Preprints (www.preprints.org) | NOT PEER-REVIEWED | Posted: 9 October 2020 doi:10.20944/preprints202010.0200.v1

3.2 Effect of head position and extra-cerebral tissue enhancement

The spatial relationship between the voxel grid and the head position determines the appearance of partial volumes and Gibbs ringing artefacts [16]. We simulated the impact of this effect on leakage mapping by analysing the error after randomising the starting head position (without intra- or inter-frame motion or noise). Qualitative results of this experiment are shown in Figure 6. The error caused by sampling the signal in *k*-space propagates differently depending on the initial head position, causing both over- and under-estimation of the actual *PS* values of median relative error 4.39 (IQR -21.44, 38.67) % and 5.84 (IQR -20.15, 40.33) % for the two initial positions.

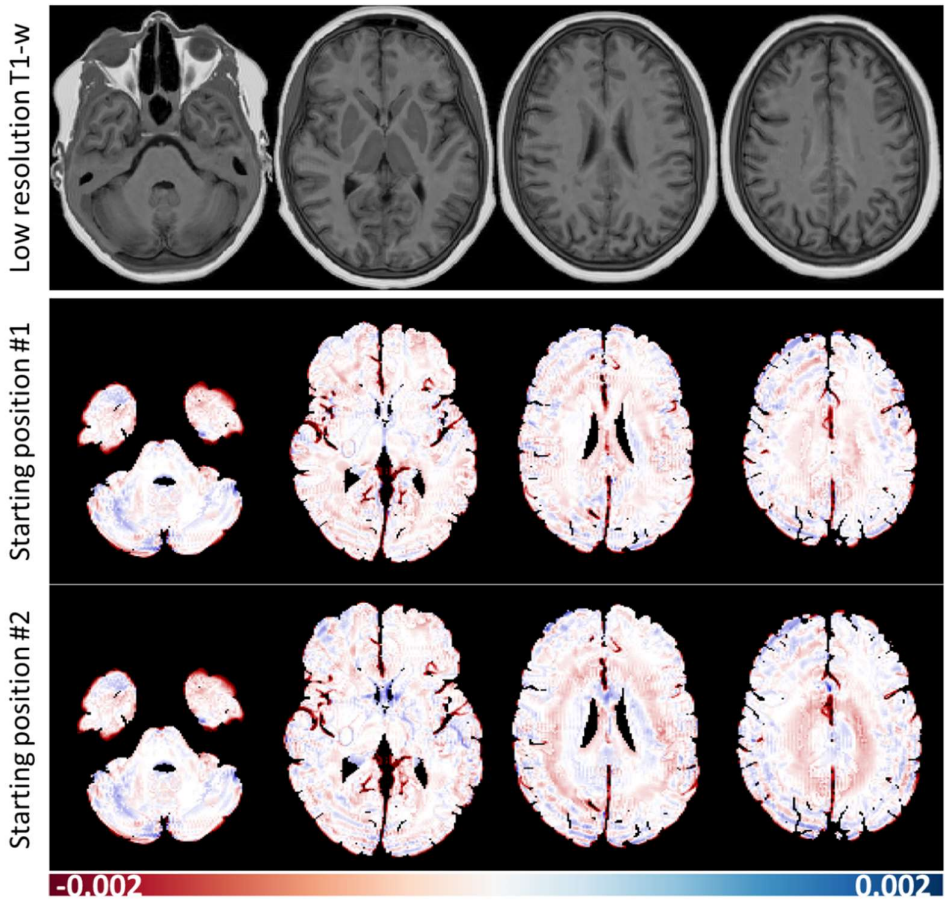

Figure 6. Error in PS mapping depending on the initial head position, quantified as the difference between the measured and true values. The error is seen to have a sinc-like distribution that depends on initial head position, consistent with k-space truncation effects. Simulations excluded motion or noise effects.

Since extra-brain tissues do not have a BBB and may therefore exhibit greater signal enhancement, we hypothesised that the boundaries of these tissues (e.g. between the inner and outer skull tables and their surroundings) contribute to the observed ringing artefacts. To examine whether this was the case, we compared the error obtained from simulations with and without non-brain signal enhancement. The qualitative results shown in Figure 7 demonstrate that extra-cerebral signal

Preprints (www.preprints.org) | NOT PEER-REVIEWED | Posted: 9 October 2020 doi:10.20944/preprints202010.0200.v1

enhancement is responsible for the observed sinc-like artefacts as they attenuated when we disabled extra-cerebral enhancement. The propagation of these ringing artefacts within brain tissues led to median relative *PS* estimation errors of 6.70 (IQR -36.71, 45.54) % versus -3.95 (IQR -22.16, 16.02) % when non-brain enhancement was absent. Residual errors persisted in tissue proximal to medium and large blood vessels. These findings were reproducible across a range of head starting positions.

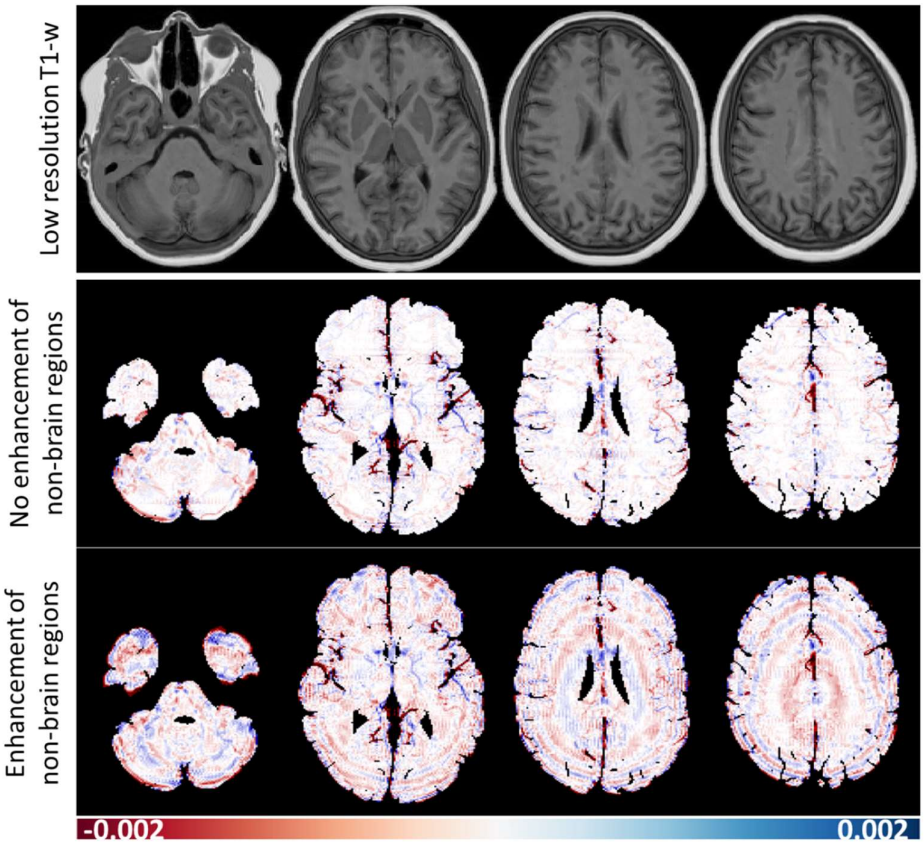

Figure 7. Error in PS mapping simulated with and without non-brain tissue enhancement. The sinc-like error distribution disappears when non-brain tissue enhancement is disabled, suggesting that such errors are caused by undersampling of the high spatial frequencies induced by non-brain enhancement. Simulations excluded motion or noise effects.

3.3 Accuracy and precision of quantitative *PS* estimation

To predict the accuracy and precision of quantitative *PS* measurements, we performed 201 simulations, using a different motion trajectory, AWGN contribution and initial orientation each time. For each run, tissue *PS* values were estimated using both a signal-averaging (i.e. modelling of the tissue-averaged signal) and parameter-averaging (i.e. averaging over the *PS* parametric map) approach. The results are shown in Figure 8 and Table 1 and 2 in the Supplementary Material. Overall, parameter map median resulted in comparable or better *PS* estimates compared with signal averaging. Both methods overestimated the *PS* values for grey matter and WMH and underestimated *PS* for NAWM and stroke lesion tissues, consistent with the single scan analyses shown in Figure 5.

Preprints (www.preprints.org) | NOT PEER-REVIEWED | Posted: 9 October 2020 doi:10.20944/preprints202010.0200.v1

Gross motion caused most of the quantification error, typically increasing both the systematic bias and the spread of values. Although incorporating both motion artefacts and additive white Gaussian noise increased the dispersion, the median value computed was not substantially affected.

Since the results described in the above sections indicate a significant error contribution from partial volume effects and non-local signal due to Gibbs ringing, we tested whether the error decreased following erosion of the segmentation masks [6] using a sphere kernel with radii equal to one voxel. The corresponding *PS* estimates showed (Figure 8) overall increased accuracy and precision following erosion, regardless of estimation method and in all tissues except stroke lesions.

Preprints (www.preprints.org) | NOT PEER-REVIEWED | Posted: 9 October 2020 doi:10.20944/preprints202010.0200.v1

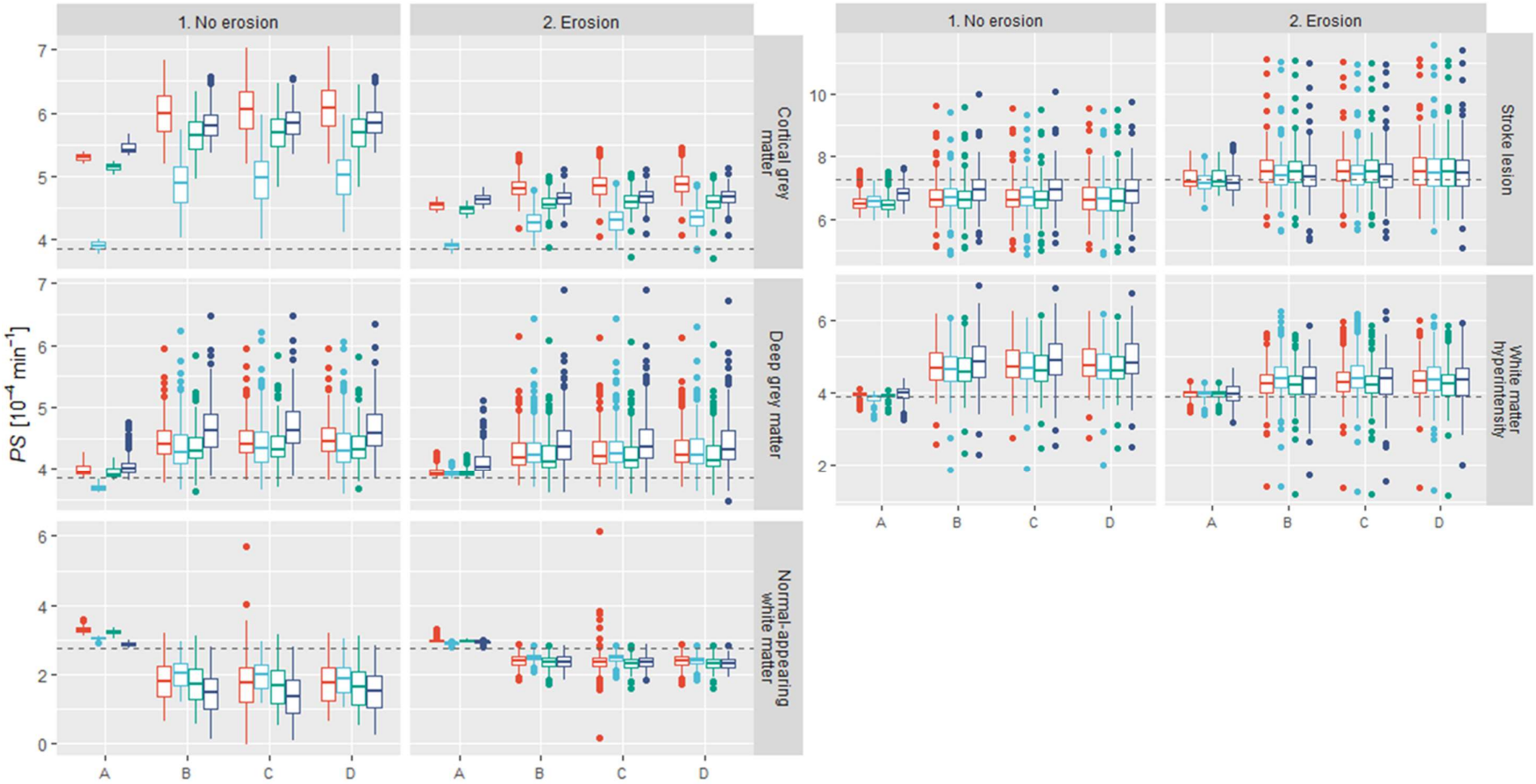

Figure 8. PS values estimated using parameter map mean (red), parameter map median (light blue), signal mean (green), and signal median (dark blue) per region of interest as we progressively induced spatio-temporal effects (A: k-space sampling only. B: sampling and gross motion. C: sampling, gross motion, and motion artefacts. D: sampling, gross motion, motion artefacts and additive white Gaussian noise). The dotted lines represent the true PS values for each tissue. For the purpose of visualisation, we exclude one outlier observation in normal-appearing white matter with PS > 0^{-3}min^{-1}.

Preprints (www.preprints.org) | NOT PEER-REVIEWED | Posted: 9 October 2020 doi:10.20944/preprints202010.0200.v1

4 Discussion

In this work, we present an open-source computational model for mimicking the DCE-MRI acquisition process for quantitative mapping of subtle BBB leakage under realistic conditions, including patient motion, anatomy and signal enhancement dynamics based on in-vivo clinical data. We found that even low levels of motion and image artefact have a large impact on both the appearance of parametric leakage maps and on quantitative measurements of leakage rates within regions of interest.

Previous simulation work has examined a number of other factors that may affect such measurements. For example, more than one research group has demonstrated the suitability of the Patlak pharmacokinetic model for measuring low-level *PS* [6], [7], [9]. The researchers also demonstrated the effects of noise, impaired cerebral blood flow, the number of pre-contrast baseline volumes acquired and the impact of scanner drift on the accuracy and precision of *PS* measurements. While such findings have provided essential insights and informed guidance regarding optimal acquisition and processing strategies [4], they are based on simulations of one-dimensional time-signal data and, thus, do not address spatio-temporal factors, which, as we have shown here, have a substantial influence, over and above that of noise.

In summary, we scrutinised the impact of spatio-temporal effects on the appearance of leakage maps by progressively inducing them in the DRO. The first of these, *k*-space sampling, has two main consequences: partial volume averaging and Gibbs ringing artefact. While the appearance of Gibbs artefact on the source T1w images was subtle, the effect was greatly magnified in the leakage maps. This result can be understood by considering that, although the magnitude of ringing artefacts in the source images is merely a few percent of the signal intensity, such a signal contribution is similar to or larger than the signal changes caused by slow contrast agent leakage in brain tissue. The effect is particularly apparent in the partition direction, where the voxel size is lowest. Despite the Gibbs artefact, some tissue permeability differences remained apparent in the leakage maps. Inclusion of gross patient motion in the simulations further degraded the leakage maps, obscuring tissue differences and introducing artefactual features, particularly around vessels, lateral ventricles and tissue boundaries. The inclusion of motion artefact had a further impact on the quality of leakage maps, primarily in the form of ghosting and blurring features. While the incorporation of additive white Gaussian noise further degraded the appearance, the additional relative impact was small. The oval shape of some of these artefacts implies that they originate from or close to the surface of the brain, while the observed dependence on initial head position is consistent with the dependence of Gibbs artefact on the position of tissue boundaries in relation to the voxel grid [17]. Additional simulations, in which we switched off the much larger contrast enhancement occurring in some non-

 doi:10.20944/preprints202010.0200.v1

brain regions, suggest that finite *k*-space sampling of the high spatial frequencies induced by these enhancements has a notable impact on measured leakage patterns within the brain.

We also assessed the impact of the same spatio-temporal imaging factors on quantitative tissue-averaged leakage measurements. We found reasonable levels of accuracy in the absence of motion effects, with the exception of cortical grey matter and stroke lesion tissues, where sampling factors have a proportionately larger effect due to their size and morphology. Gross motion combined with *k*-space sampling had the largest effect on the accuracy and precision, consistent with the observed impact on individual leakage maps. For example, we observed a bias towards higher (27.01 [IQR 19.18, 33.23] %) and lower (-24.99 [IQR -37.6, -15.75] %) values in cortical grey matter and normal-appearing white matter, respectively. As an explanation, we propose that head motion, which is not fully corrected by spatial realignment algorithms, causes signal from neighbouring tissues to “enter” any given tissue mask; since tissues have different T1w signal intensities, this results in a time-dependent signal change that affects leakage estimates. Simulation of motion artefact and image noise was shown to have a much smaller effect.

Our work has implications for the analysis and interpretation of DCE-MRI subtle leakage data. First, the use of an appropriate pharmacokinetic model, temporal resolution and sufficiently high signal-to-noise ratio are essential but not sufficient conditions to obtain reliable results, since spatio-temporal considerations have a major impact on the accuracy and precision. Secondly, leakage maps in individual patients may be an unreliable source of information, as they are highly distorted by imaging artefacts and motion; such maps should be interpreted with caution, since artefactual leakage features are likely to be present, even (as simulated here) if the true leakage rate is uniform within each tissue. Therefore, it is important to acknowledge that apparent features such as leakage “hotspots”, “rims”, negative leakage rates and shifts in the distribution can be caused by patient motion and data sampling effects. This consideration is particularly relevant to studies of ageing where key pathological features, namely periventricular WMH, may coincide with regions where the artefact level is high. Post-processing techniques designed to denoise leakage maps or identify voxels with significant leakage [5], [18], [19] could also be potentially confounded by these effects, which distort the central value, width and shape of the voxel leakage distribution. Quantitative leakage rates estimated for each tissue may also be subject to substantial systematic biases and random error as a result of these effects. Since the degree of patient motion is likely to be related to severity of neurodegenerative disease, there is therefore a possibility of inferring false associations between leakage rate and disease. Thirdly, by applying suitable post-processing techniques, namely erosion of tissue segmentation masks, the accuracy obtained in most tissues can be improved by reducing contamination from neighbouring tissues. However, the potential benefit should be balanced against

 doi:10.20944/preprints202010.0200.v1

the severe reduction in signal averaging for regions with high surface-area-to-volume ratio. Fourthly, we observed similar accuracy and precision regardless of whether averaging was performed over the parameter maps or over the MR image, except in cortical grey matter, where median parametric values yielded the greatest accuracy.

Our work also has implications for future development of the technique and the design of future studies targeting subtle BBB leakage. The computation framework for generating DROs presented here, which is freely available as source code, provides a convenient means to evaluate and compare proposed DCE-MRI protocols including the influence of spatial and temporal resolution parameters. The critical impact of motion revealed by our experiments also argues for evaluating motion-resistant acquisition techniques, such as optical prospective motion compensation, provided temporal resolution, signal stability and other key technical elements are not compromised. Equally, the value of post-processing techniques, such as spatial realignment, and retrospective spatial artefact reduction methods targeting truncation [16] and motion artefacts can now also be explored.

Our work has some limitations. First, although the DROs are generated using a high-resolution (0.5-mm isotropic) brain atlas to synthesise the MRI signal, it may not be sufficient to model all anatomical structures and tissue boundaries accurately. To our knowledge, the MIDA atlas is the highest resolution head and neck atlas with comprehensive labelling available at present, however higher resolution (e.g. based on 7-T MRI) atlases could be used in future. Second, we simulated data using a number of necessary assumptions and simplifications. For example, dynamic brain tissue signals were generated using the Patlak model, since this ensures that any errors we identified are a consequence of the spatio-temporal factors investigated here and not due to physiological limitations of the model, which have been investigated extensively elsewhere. Third, our technique for simulating motion effects resulted in motion artefacts with realistic appearance within an acceptable computation time; simulating continuous patient motion throughout the acquisition would generate more realistic data but at the cost of increased computation time. Fourth, the results presented herein correspond to a specific DCE-MRI protocol and would likely be quantitatively different for a different protocol. Nevertheless, the protocol simulated is typical of those described in the literature, concerning spatial resolution, acquisition time and pulse sequence. It would be straightforward to simulate alternative protocols and pulse sequences (e.g. saturation recovery spoiled gradient echo) using our framework. Fifth, we simulated a DRO including small vessel disease features seen in the ageing brain, such as WMH and stroke lesions. However, study populations typically comprise a range of disease burdens and other features, such as lacunes, enlarged perivascular spaces, micro-haemorrhages (i.e., micro-bleeds), sulcal widening and ventricular enlargement among others; future work could address the impact of brain ageing and neurovascular health on the accuracy of leakage measurements.

Preprints (www.preprints.org) | NOT PEER-REVIEWED | Posted: 9 October 2020 doi:10.20944/preprints202010.0200.v1

In conclusion, we have developed and made publicly-available a novel DRO for simulating DCE-MRI measurement of subtle BBB leakage (https://github.com/joseabernal/BrainDCEDRO). This development is timely, given the rapidly growing interest in neurodegenerative diseases, such as small vessel disease and dementia, which are linked with subtle BBB dysfunction, and the growing interest in applying DCE-MRI in this area. Our work reveals reasons to be careful when interpreting such data, and provides a means to estimate and optimise the reliability of measurements.

5 Data and code availability statement

We implemented our computational model in MATLAB R2018 Update 4 (9.5.0.1067069). We have made our source code and motion trajectories publicly available in GitHub: github.com/joseabernal/BrainDCEDRO. The MIDA model used in this work can be downloaded from the following URL: www.itis.ethz.ch/MIDA. Our code requires downloading two additional open-source packages to run: github.com/mjt320/DCE-functions and github.com/mjt320/utilities. We produced Figures 5 and 8 using RStudio 1.2.5019 with R v3.5.1, and have provided the raw data and scripts for generating them as supplementary material.

6 CRediT authorship contribution statement

Jose Bernal: conceptualisation, methodology, software, formal analysis, investigation, writing – original draft preparation, writing – review and editing, visualisation. **Maria d. C. Valdés-Hernández**: resources, data curation, writing – review and editing, supervision, funding acquisition. **Javier Escudero**: resources, data curation, writing – review and editing, supervision, funding acquisition. **Anna K. Heye**: data curation, writing – review and editing. **Eleni Sakka**: data curation, writing – review and editing. **Paul A. Armitage**: data curation, writing – review and editing. **Stephen Makin**: data curation, writing – review and editing. **Rhian M. Touyz**: resources, writing – review and editing, supervision, funding acquisition. **Joanna M. Wardlaw**: resources, data curation, writing – review and editing, supervision, funding acquisition. **Michael J. Thrippleton**: conceptualisation, methodology, software, validation, formal analysis, investigation, project administration, writing – original draft preparation, writing – review and editing, supervision.

7 Conflict of interest

The authors declare no conflict of interest. The funders had no role in the design of the study; in the collection, analyses, or interpretation of data; in the writing of the manuscript, or in the decision to publish the results.

Acknowledgements

This work is supported by the UK Dementia Research Institute, which receives its funding from DRI Ltd, funded by the UK MRC, Alzheimer's Society, and Alzheimer's Research UK; the Wellcome Trust (patient recruitment, scanning, and primary study - Reference No. WT088134/Z/09/A); the Fondation Leducq Network for the Study of Perivascular Spaces in Small Vessel Disease (16 CVD 05); The Row Fogo Charitable Trust Centre for Research into Aging and the Brain (MVH) (BRO-D.FID3668413); a British Heart Foundation Chair award (RMT) (CH/12/4/29762); NHS Lothian Research and Development Office (MJT); European Union Horizon 2020, PHC-03-15, project No666881; and the MRC Doctoral Training Programme in Precision Medicine (JB). We thank the participants, their families, radiographers at the Edinburgh Imaging Facility Royal Infirmary of Edinburgh, and the Stroke Research Network at the University of Edinburgh.

References

[1] J. M. Wardlaw *et al.*, "Blood-brain barrier failure as a core mechanism in cerebral small vessel disease and dementia: evidence from a cohort study," *Alzheimer's Dement.*, vol. 13, no. 6, pp. 634–643, 2017.

[2] A. Montagne *et al.*, "APOE4 leads to blood–brain barrier dysfunction predicting cognitive decline," *Nature*, vol. 581, no. 7806, pp. 71–76, 2020.

[3] J. M. Wardlaw, C. Smith, and M. Dichgans, "Small vessel disease: mechanisms and clinical implications," *Lancet Neurol.*, vol. 18, no. 7, pp. 684–696, 2019.

[4] M. J. Thrippleton *et al.*, "Quantifying blood-brain barrier leakage in small vessel disease: Review and consensus recommendations," *Alzheimer's Dement.*, vol. 44, no. 6, pp. 1–19, 2019.

[5] R. Raja, G. A. Rosenberg, and A. Caprihan, "MRI measurements of Blood-Brain Barrier function in dementia: A review of recent studies," *Neuropharmacology*, vol. 134, pp. 259–271, 2018.

[6] A. K. Heye *et al.*, "Tracer kinetic modelling for DCE-MRI quantification of subtle blood-brain barrier permeability," *Neuroimage*, vol. 125, pp. 446–455, 2016.

[7] S. R. Barnes, T. S. C. Ng, A. Montagne, M. Law, B. V. Zlokovic, and R. E. Jacobs, "Optimal acquisition and modeling parameters for accurate assessment of low Ktrans blood-brain barrier permeability using dynamic contrast-enhanced MRI," *Magn. Reson. Med.*, vol. 75, no. 5, pp. 1967–1977, 2016.

[8] P. A. Armitage, A. J. Farrall, T. K. Carpenter, F. N. Doubal, and J. M. Wardlaw, "Use of dynamic contrast-enhanced MRI to measure subtle blood-brain barrier abnormalities," *Magn. Reson. Imaging*, vol. 29, no. 3, pp. 305–314, 2011.

[9] S. P. Cramer and H. B. W. Larsson, "Accurate determination of blood-brain barrier permeability using dynamic contrast-enhanced T1-weighted MRI: A simulation and in vivo study on healthy subjects and multiple sclerosis patients," *J. Cereb. Blood Flow Metab.*, vol. 34, no. 10, pp. 1655–1665, 2014.

[10] M. I. Iacono *et al.*, "MIDA: A multimodal imaging-based detailed anatomical model of the human head and neck," *PLoS One*, vol. 10, no. 4, 2015.

[11] C. S. Patlak and R. G. Blasberg, "Graphical evaluation of blood-to-brain transfer constants from multiple-time uptake data. Generalizations," *J. Cereb. Blood Flow Metab.*, vol. 5, no. 4, pp. 584–590, 1985.

[12] H. B. W. Larsson, F. Courivaud, E. Rostrup, and A. E. Hansen, "Measurement of brain perfusion, blood volume, and blood-brain barrier permeability, using dynamic contrast-enhanced T1-weighted MRI at 3 tesla," *Magn. Reson. Med.*, vol. 62, no. 5, pp. 1270–1281, 2009.

[13] R. Shaw, C. H. Sudre, T. Varsavsky, S. Ourselin, and M. J. Cardoso, "A k-Space Model of Movement Artefacts: Application to Segmentation Augmentation and Artefact Removal," *IEEE Trans. Med. Imaging*, vol. 0062, no. c, pp. 1–1, 2020.

[14] M. Jenkinson, P. Bannister, M. Brady, and S. Smith, "Improved optimization for the robust and accurate linear registration and motion correction of brain images," *Neuroimage*, vol. 17, no. 2, pp. 825–841, 2002.

[15] M. del C. Valdés Hernández *et al.*, "Rationale, design and methodology of the image analysis protocol for studies of patients with cerebral small vessel disease and mild stroke," *Brain Behav.*, vol. 5, no. 12, pp. 1–8, 2015.

[16] E. Kellner, B. Dhital, V. G. Kiselev, and M. Reisert, "Gibbs-ringing artifact removal based on local subvoxel-shifts," *Magn. Reson. Med.*, vol. 76, no. 5, pp. 1574–1581, 2016.

[17] P. Ferreira, P. Gatehouse, P. Kellman, C. Bucciarelli-Ducci, and D. Firmin, "Variability of myocardial perfusion dark rim Gibbs artifacts due to sub-pixel shifts," *J. Cardiovasc. Magn. Reson.*, vol. 11, no. 1, pp. 1–10, 2009.

[18] H. J. van de Haar *et al.*, "Blood-Brain Barrier Leakage in Patients with Early Alzheimer Disease," *Radiology*, vol. 282, no. 2, pp. 615–615, 2017.

[19] S. Taheri *et al.*, "Blood-brain barrier permeability abnormalities in vascular cognitive impairment.," *Stroke*, vol. 42, no. 8, pp. 2158–63, 2011.